Porous alumina nanosheets supported asymmetric platinum clusters for efficient diboration of alkynes

Yan Gao,‡[a] Huilong Geng,‡[b] Jinlong Ge,[a] Linlin Zhu,[a] Zhiyi Sun,[b] Ziwei Deng[b] and Wenxing Chen*[b]

Chemicals.

Analytical grade Aluminium chloride ($AlCl_3$), Magnesium powder (Mg), 1-Butanesulfonic acid sodium salt (BSAC) and Chloroplatinic acid ($H_2PtCl_6 \cdot 6H_2O$) were obtained from Sinopharm Chemical Reagent Co.,Ltd. Bis (pinacolato)diboron (B_2pin_2) was purchased from Sigma-Aldrich. Methylbenzene and phenylacetylene were purchased from Innochem. All the materials were used as received without further purification.

Synthesis.

Preparation of defect porous Al_2O_3 nanosheets (dp-Al_2O_3).

$AlCl_3$ (1.5 mmol, 199.9 mg) was dissolved in deionized water (15 mL) and then mixed with an aqueous solution of Mg powder (2 mmol, 48.6 mg), BSAC (2 mmol, 0.27g) in deionized water (30 mL). After vigorous stirring for 30 min at ambient temperature, the mixture was transferred into a 50 mL Teflon-lined stainless-steel autoclave and heated at 200 °C for 3 h. The white product was collected via centrifugation and further washed with deionized water and ethanol for two times, respectively. After vacuum freeze-drying, the AlOOH nanosheets were obtained. Then, the resulting powder was placed into the tube furnace and heated to the desired temperature 500 °C for 120 min at the heating rate of 2 °C/min in Air. After cooling to room temperature, the dp-Al_2O_3 was used for characterization and further preparation without further purification.

Preparation of Pt clu/dp-Al_2O_3 catalyst.

The as-synthesized Al_2O_3 (100.0 mg) were first dispersed in 20 mL ethanol under ultrasonic vibration. A $H_2PtCl_6 \cdot 6H_2O$ solution (1mg/ml) was next added dropwise into the Al_2O_3 dispersion under stirring at ambient temperature. After continuous stirringovernight, the suspension was centrifuged. The recovered solid was then dried in vacuum oven and reduced in 5% H_2/N_2 at 200 °C for 3 h to afford the Pt clu/dp-Al_2O_3 catalyst for further characterization and catalysis test.

Preparation of the Pt NPs/c-Al_2O_3 catalyst.

The Pt NPs/c-Al_2O_3 was synthesized through the same procedure of the fabrication of Pt clu/dp-Al_2O_3 catalyst except with a commercial Al_2O_3 support instead.

Characterization.

The morphology and size of the catalyst was characterized and observed by HITACHI H7650 transmission electron microscope (TEM) with the working voltage of 80 kV. High resolution transmission electron microscope (HRTEM) was performed

by FEI Tecnai G2 F20 S-Twin with the 200 kV operating voltage and collected the elemental mappings with the assistance of X-ray energy dispersive spectroscopy detector. The crystalline structure and phase purity were identified using a D8 ADVANCE X X-ray powder diffractometer with CuKa radiation (λ = 1.5406 Å). The central metal loading of the Pt clu/dp-Al_2O_3 were measured by Agilent ICP-OES 730. X-ray photoelectron spectroscopy (XPS) was obtained by PerkinElmer Physics PHI 5300 energy spectrometer using mono-chromatic Al Kα radiation (1486.7 eV).

Catalysis testing.

In a typical procedure, alkynes (0.5 mmol, 0.5 equiv.), B_2pin_2 (0.5 mmol), Pt species catalysts (Pt 0.0005 equiv.) and methylbenzene (3 mL) were sequentially added in a 20 mL standard Schlenk tube equipped with a stir bar, then the mixture was heated at 100 ℃ and vigorously stirred for 6 hours. When the reaction was over, the yield of reaction was determined by GC and GC-MS with dodecane as the internal standard. The TOF values were calculated upon completion of reactions and based on the total Pt loading in the catalysts.

XAFS measurements.

XAFS spectra at Pt L_3-edge were collected at the 1W1B station in Beijing Synchrotron Radiation Facility in a fluorescence mode, Pt foil, PtO_2 were used as references. The k^3-weighted EXAFS spectra were obtained by subtracting the post-edge background from the overall absorption and then normalizing with respect to the edge-jump step. Subsequently, k^3-weighted χ (k) data in the k space ranging from 2.0-12.0 $Å^{-1}$ were Fourier transformed to real (R) space using hanning windows (dK = 1.0 $Å^{-1}$) to separate the EXAFS contributions from different coordination shell.

XAFS Analysis and Results.

The acquired EXAFS data were processed according to the standard procedures by using the ATHENA module of the IFEFFIT software packages. The detailed fitting process is stated below:

The obtained EXAFS spectra underwent the subtraction of post-edge background from the overall absorption and then normalization with respect to the edge-jump step. Subsequently, the χ(k) data were Fourier transformed to real (R) space by using a hanning windows (dk=1.0 $Å^{-1}$) to separate the EXAFS contributions from different coordination shells. To obtain the quantitative structural parameters around central atoms, least-squares curve parameter fitting was conducted by using the ARTEMIS module of the IFEFFIT software packages.

The following EXAFS equation was used:

$$\chi(k)=\sum_j \frac{N_j S_o^2 F_j(k)}{k R_j^2}\exp[-2k^2\sigma_j^2]\exp[\frac{-2R_j}{\lambda(k)}]\sin[2kR_j+\phi_j(k)]$$

In the equation, S_0^2 represent the amplitude reduction factor, $F_j(k)$ is the effective curved-wave backscattering amplitude, N_j is the number of neighbors in the j^{th} atomic shell, R_j represent the distance between the X-ray absorbing central atom and the atoms in the j^{th} atomic shell (backscatterer), λ represent the mean free path in Å, σ_j is the Debye-Waller parameter of the j^{th} atomic shell (variation of distances around the average R_j) and $\phi_j(k)$ is the phase shift (including the phase shift for each shell and the total central atom phase shift). The functions $F_j(k)$, λ and $\phi_j(k)$ were calculated with the ab initio code FEFF8.2

The coordination numbers of model samples (Ni foil) were fixed as the nominal values. The obtained S_0^2 was fixed in the subsequent fitting of Pt clu/dp-Al_2O_3 sample. While the internal atomic distances R, Debye-Waller factor σ^2, and the edge-energy shift ΔE_0 were allowed to run freely.

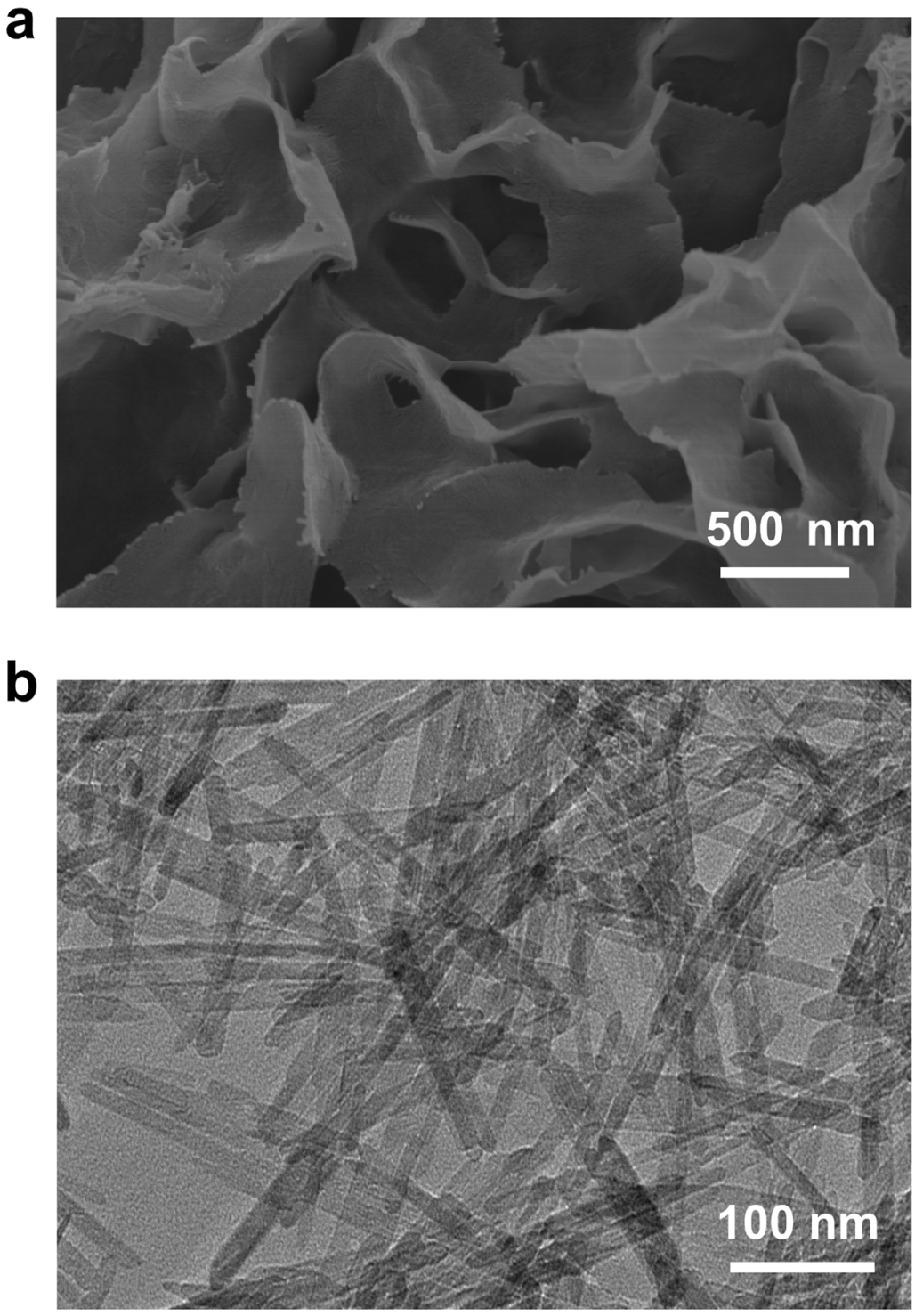

Figure S1. (a) SEM and (b) TEM image of AlOOH.

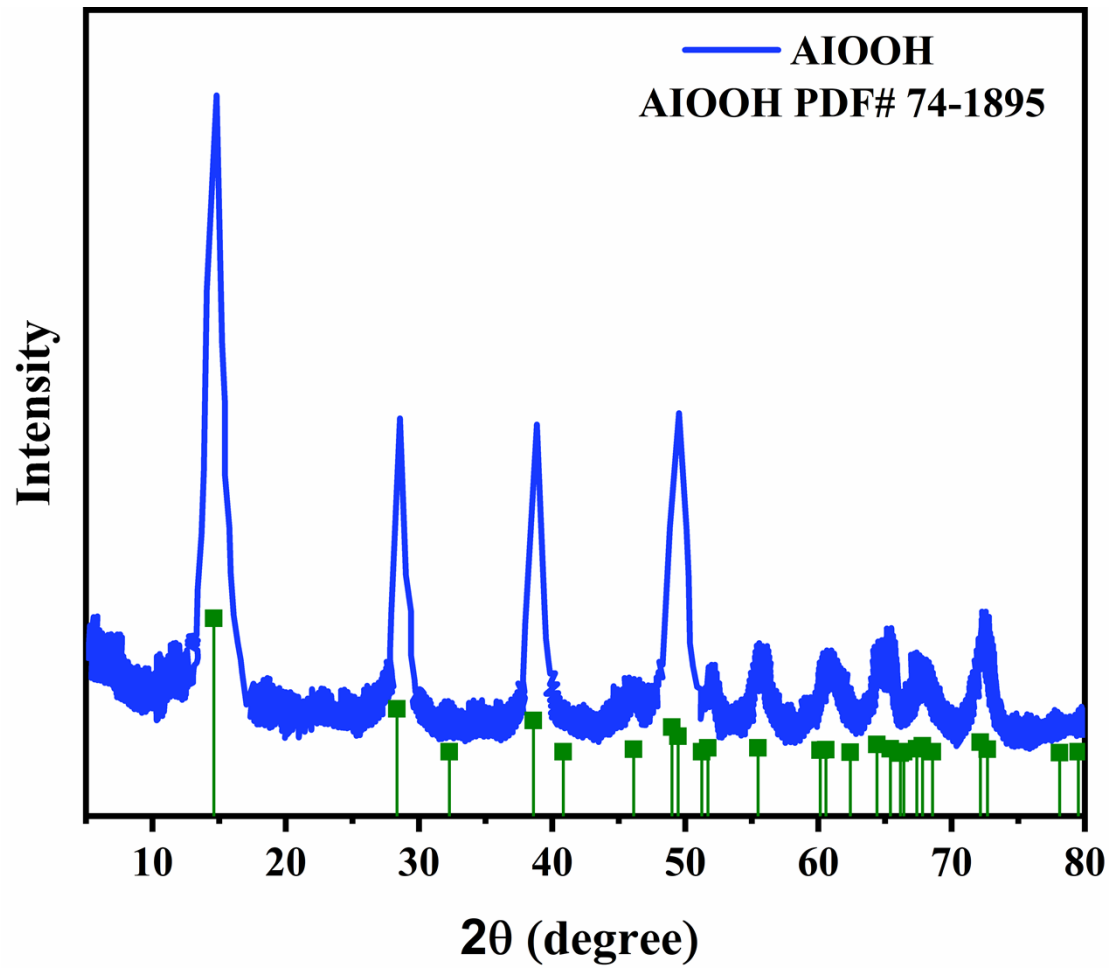

Figure S2. XRD pattern of AlOOH.

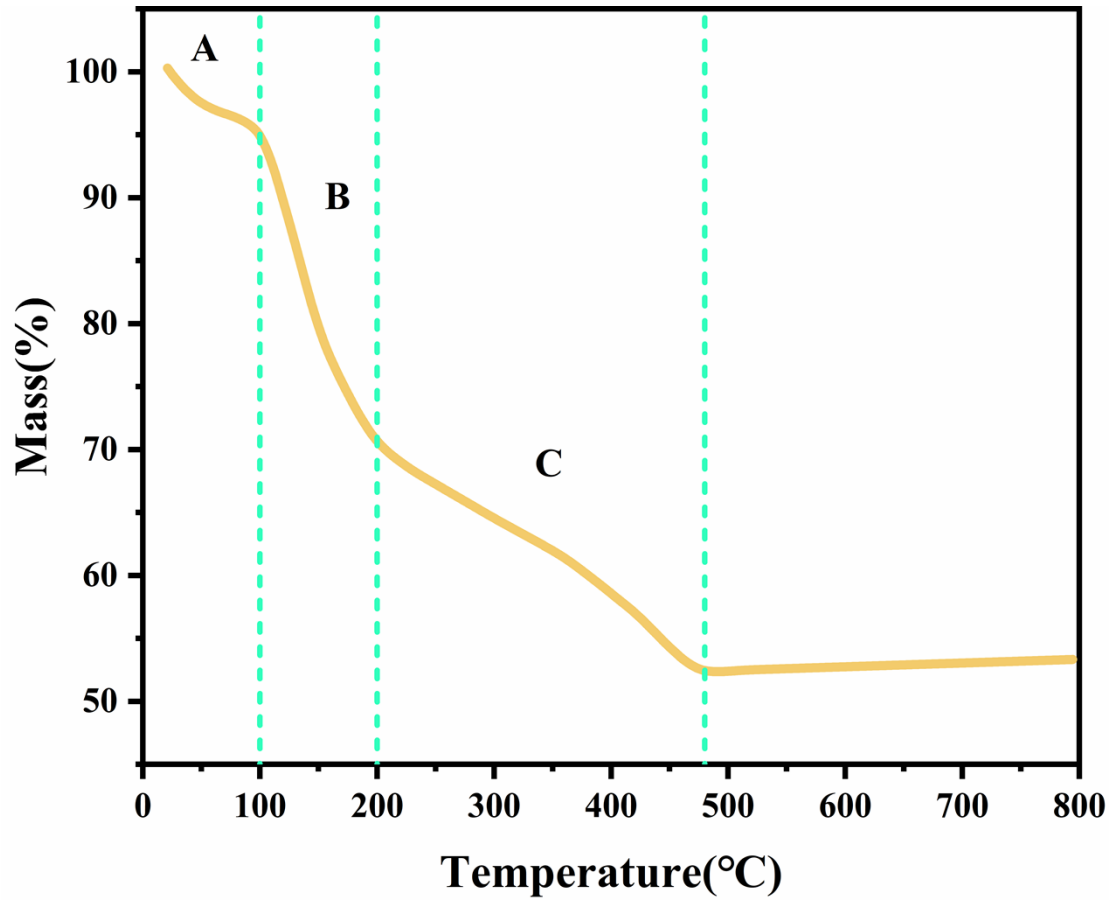

Figure S3. TGA curve of AlOOH in air from 25 °C to 800 °C.

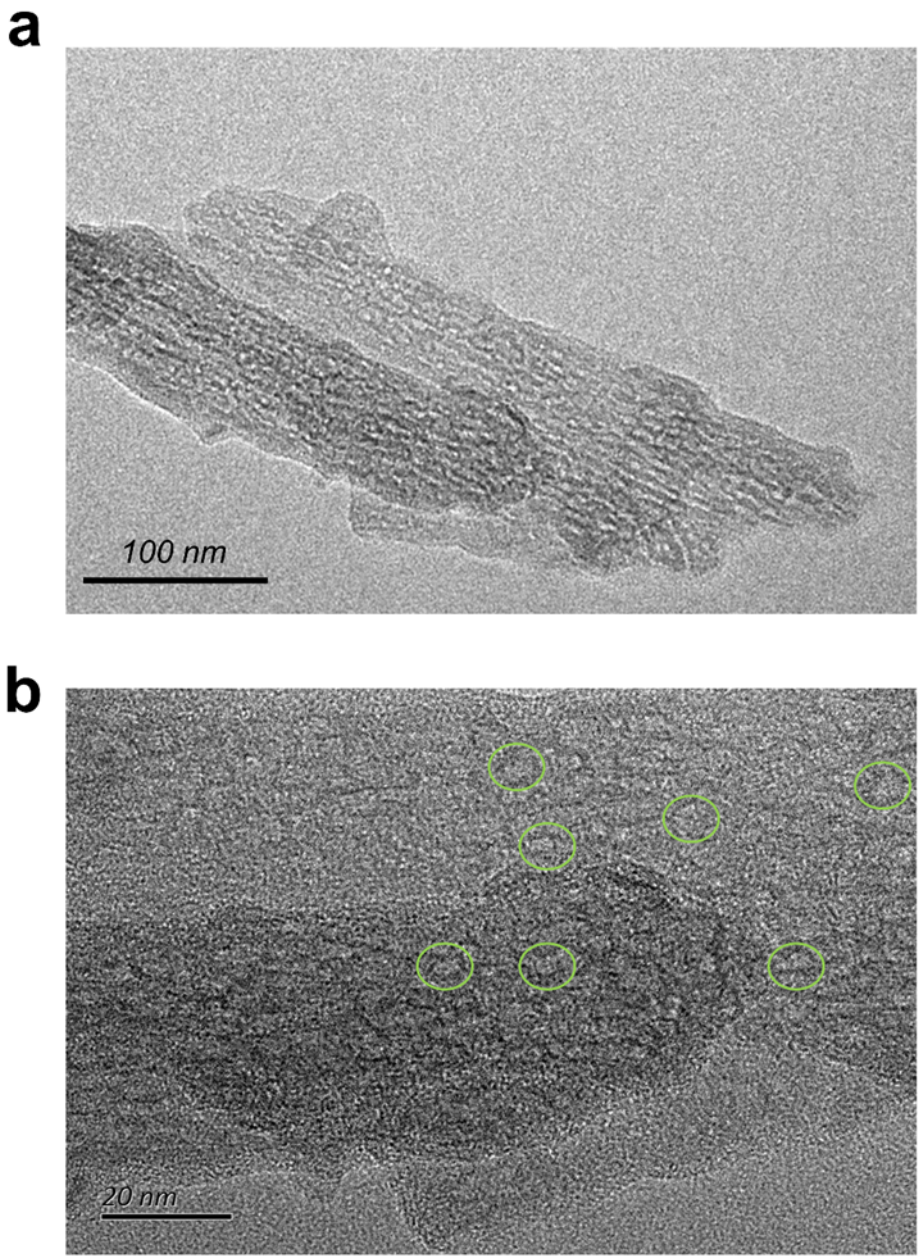

Figure S4. HRTEM images of porous defect alumina sheets. The porous structure can be seen from the image. It can be seen from HRTEM images that there are many uneven polygon defects on the surface of nanosheets.

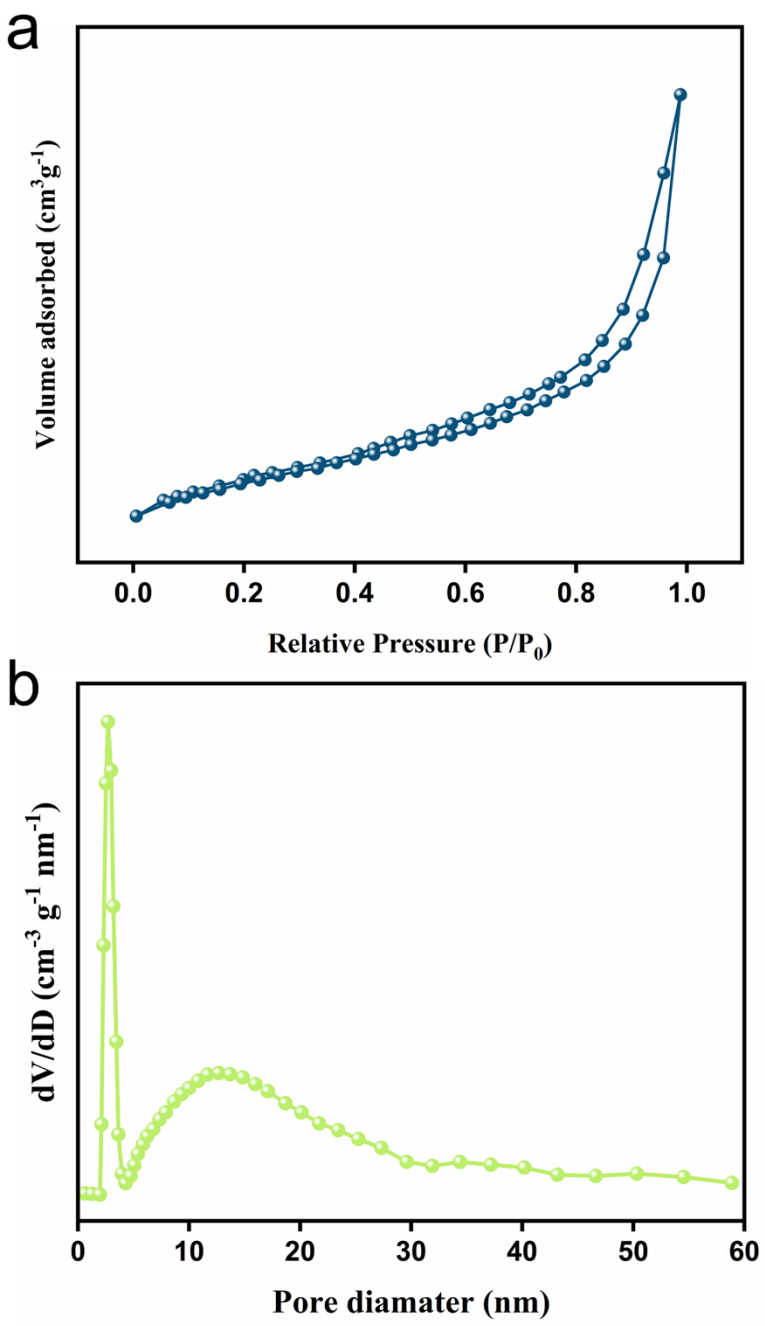

Figure S5. N_2 adsorption-desorption isotherms of dp-Al_2O_3 and the corresponding pore-size distribution curve.

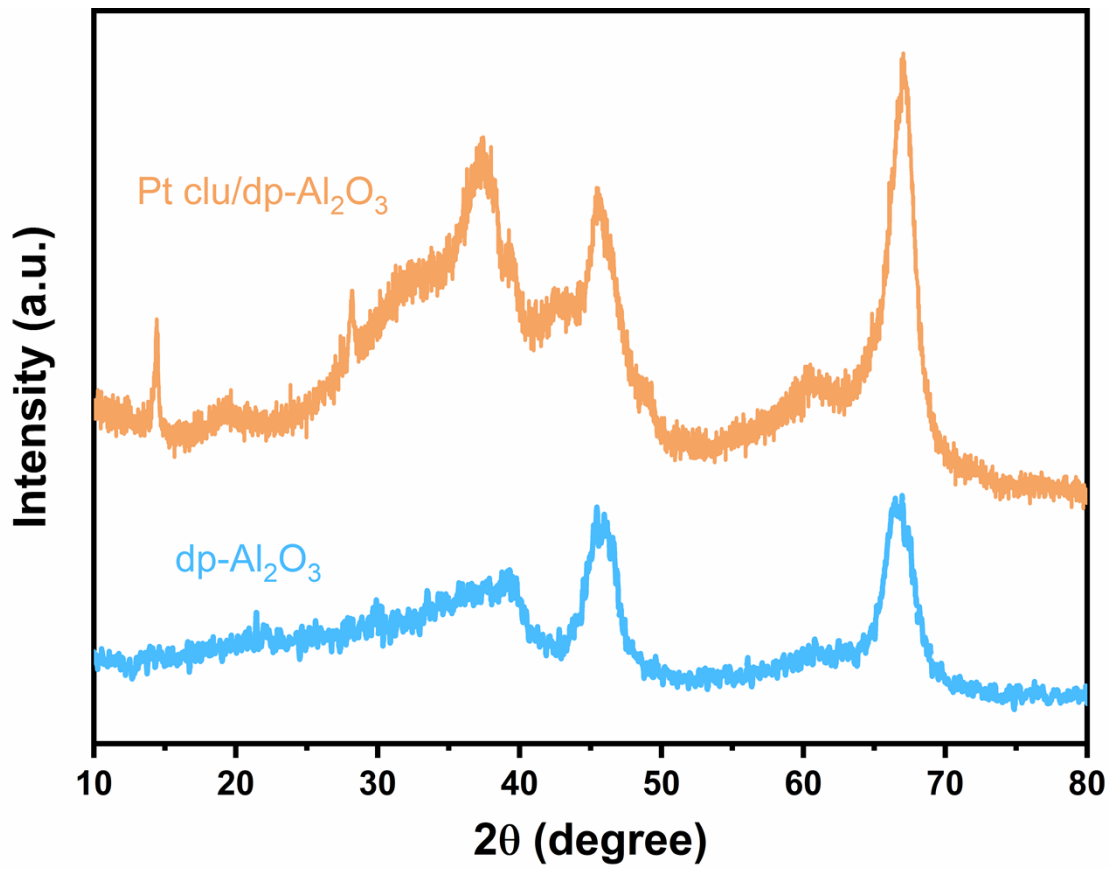

Figure S6. XRD patterns of dp-Al_2O_3, Pt clu/dp-Al_2O_3.

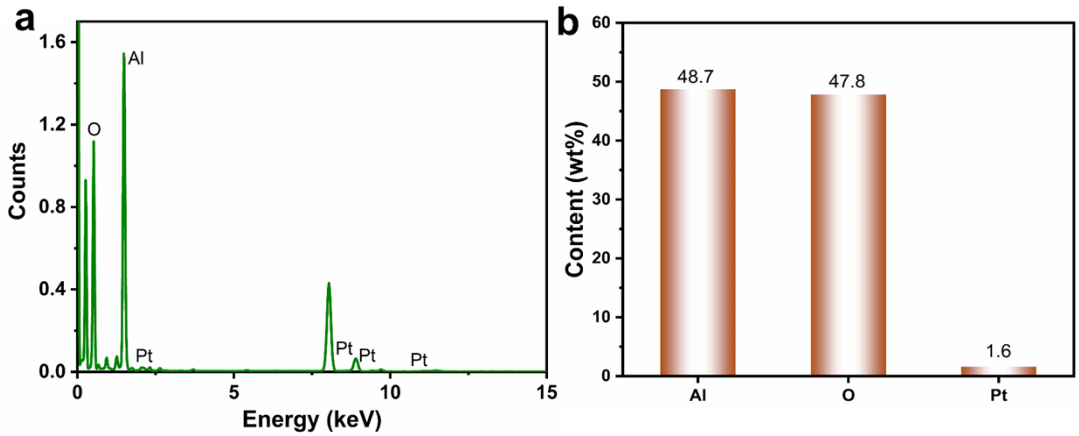

Figure S7. (a) EDS spectrum of Pt clu/dp-Al_2O_3. (b) The weight content percentages of Al, O and Pt in Pt/dp-Al_2O_3 measured by EDS analysis.

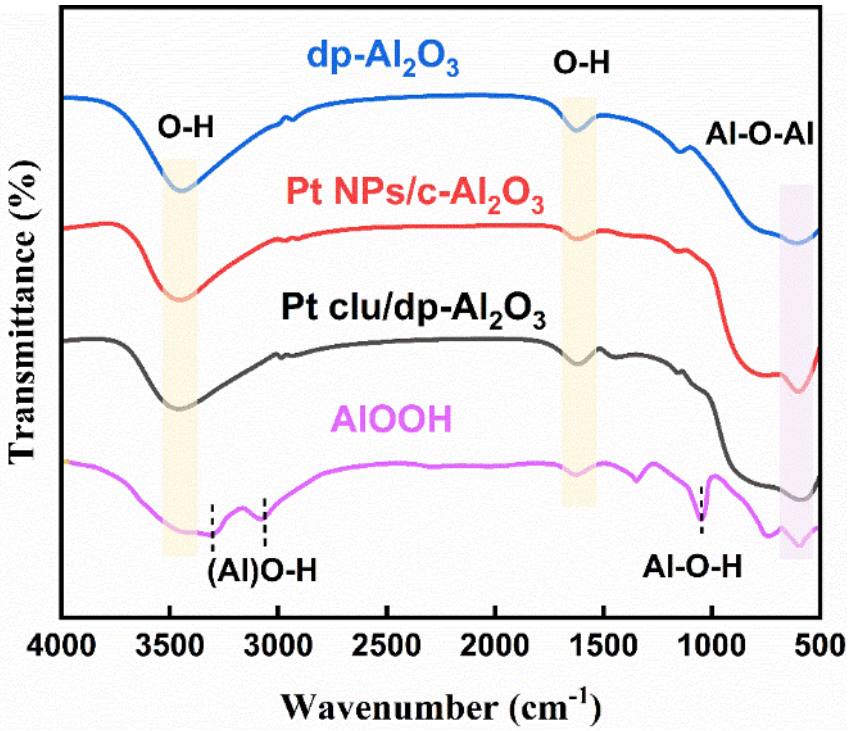

Figure S8. FT-IR spectra of dp-Al_2O_3, Pt clu/dp-Al_2O_3, Pt NPs/c-Al_2O_3 and AlOOH. The bands at 3447 and 163 cm^{-1} can be assigned to the O–H vibration of hydrogen-bonded hydroxyl groups from the metal hydroxide and intercalated water molecule. The peak at 574 cm^{-1} corresponds to the Al-O-Al vibrations. The band at 1070 cm^{-1} corresponds to the stretching vibrations of Al-O-H. Thermal decomposition of AlOOH at 500 °C, the band corresponding to (Al)O-H and Al-O-H vanished. Above data confirms the successful phase transformation of AlOOH to the Al_2O_3.

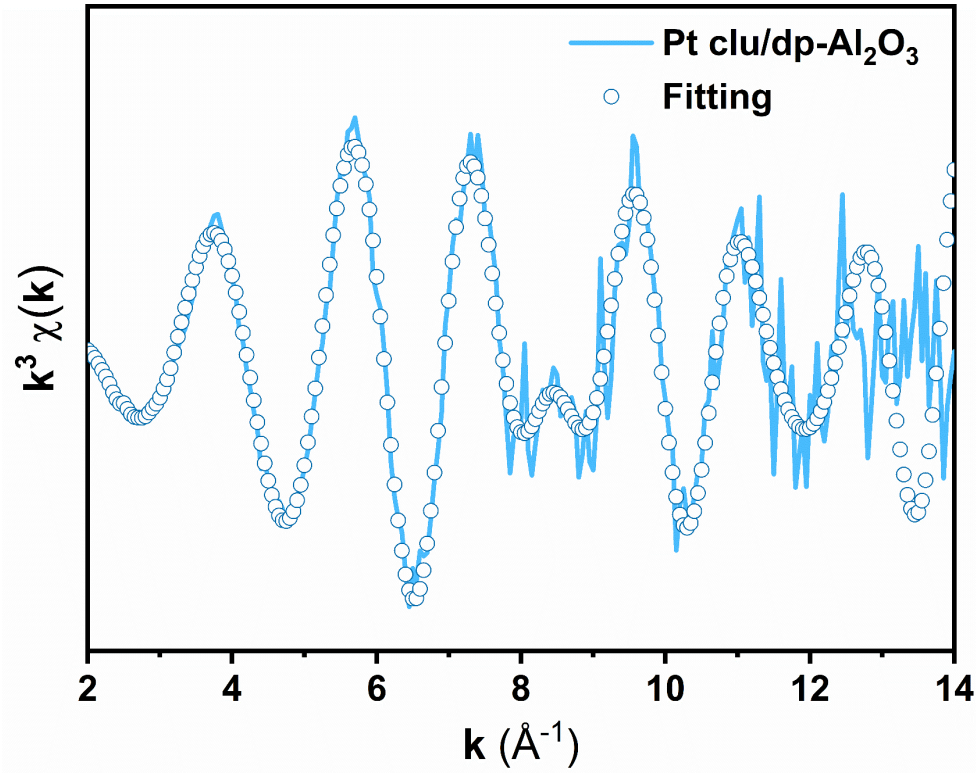

Figure S9. (a) k space EXAFS fitting curves of the Pt clu/dp-Al_2O_3.

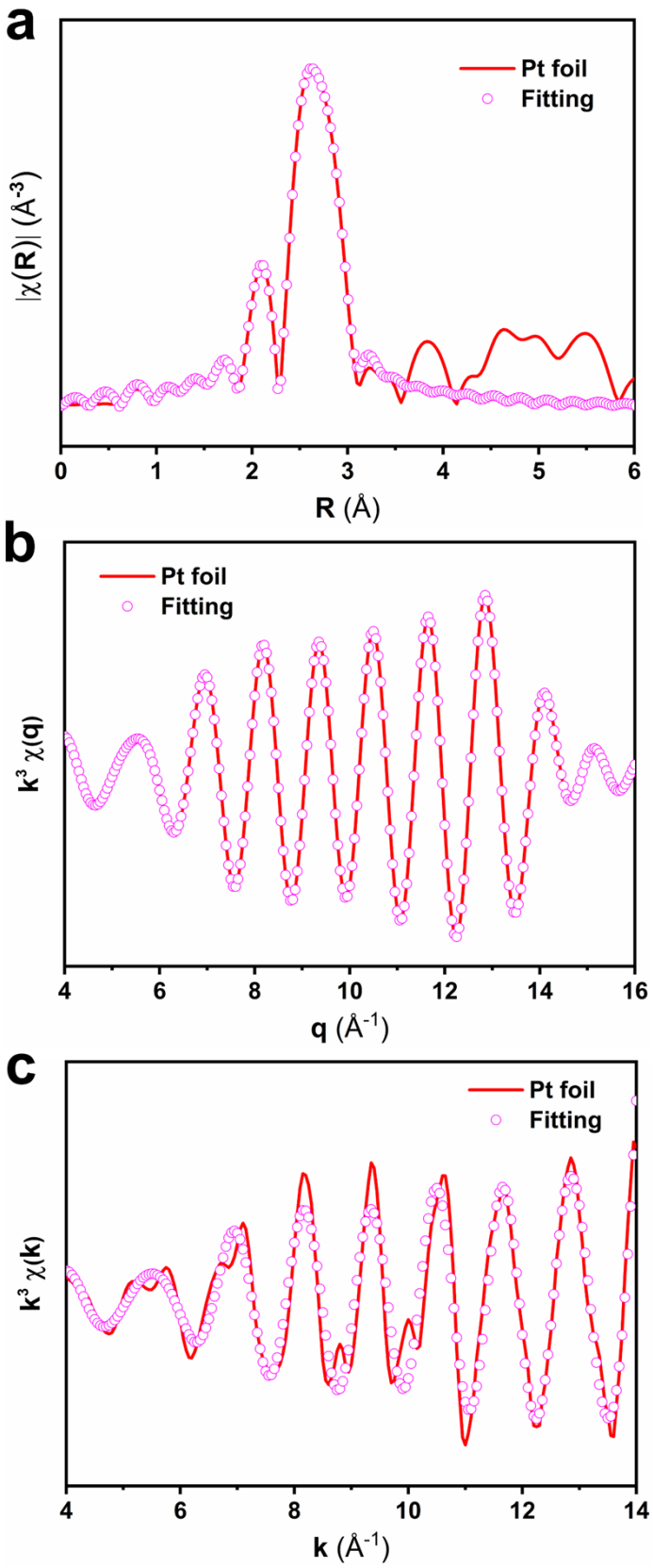

Figure S10. The EXAFS fitting results of Pt foil at (a) R, (b) q and (c) k space. Pt foil (FT range: 2.0-13.8 $Å^{-1}$; fitting range: 1.8-3.2 Å).

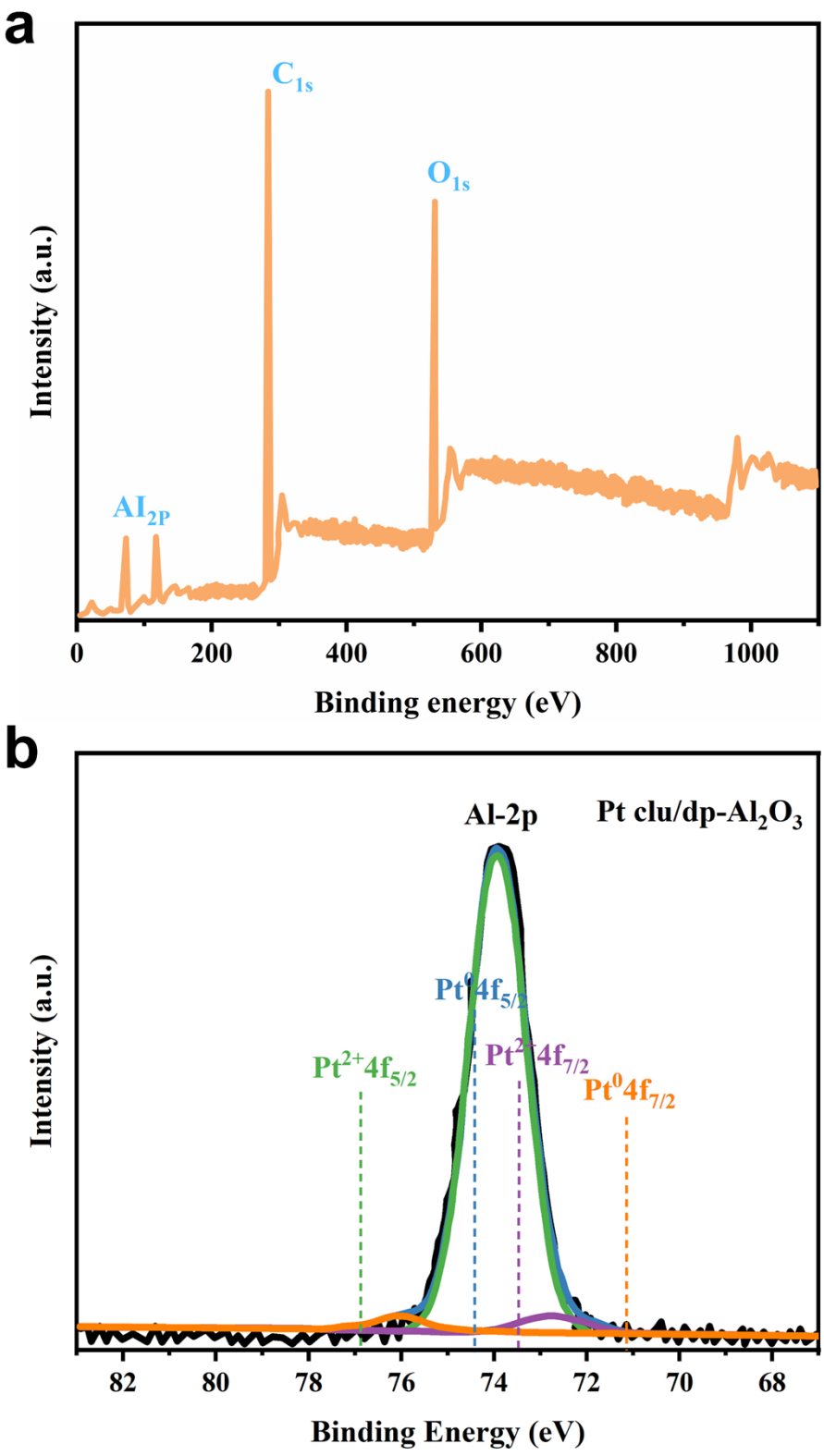

Figure S11. XPS spectra for the survey scan (a) and Al 2P, Pt 4f region of Pt clu/dp-Al_2O_3 (b).

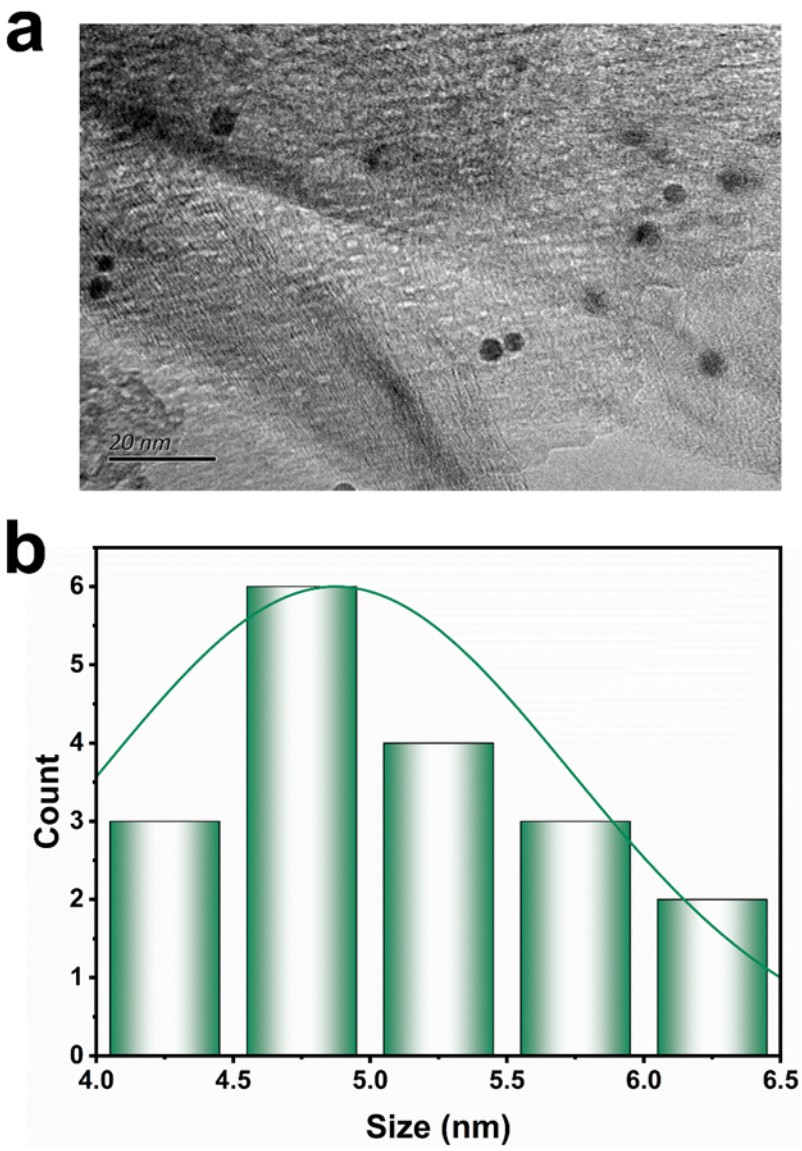

Figure S12. (a) TEM images of Pt NPs/c-Al_2O_3. (b) Size distribution of Pt particles. It is distinctly observed that plenty of Pt nanoparticles. The size distribution of the measured Pt species ranged from 3.42 nm to 6.21 nm. The average Pt particle size is estimated at 4.68 nm.

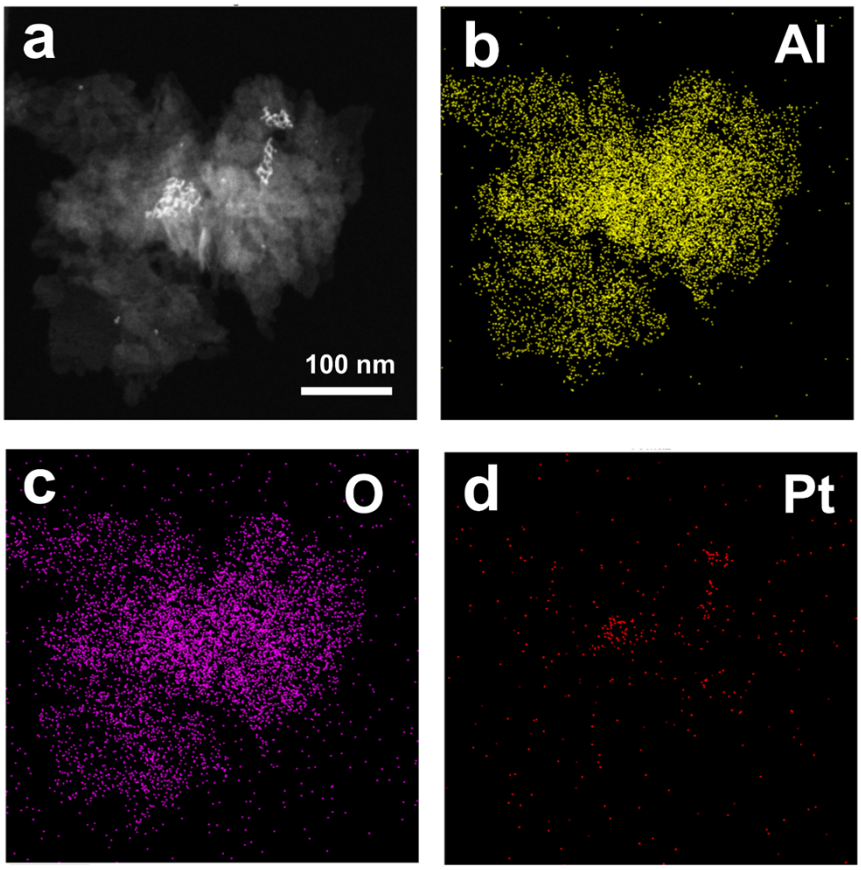

Figure S13. The structural characterizations of the Pt clu/dp-Al_2O_3 catalyst after recycle text. (a) the HAADF-STEM images of Pt clu/dp-Al_2O_3. (b-d) EDS elemental mapping images of Pt clu/dp-Al_2O_3 (Al: yellow, O: pink, Pt: red).

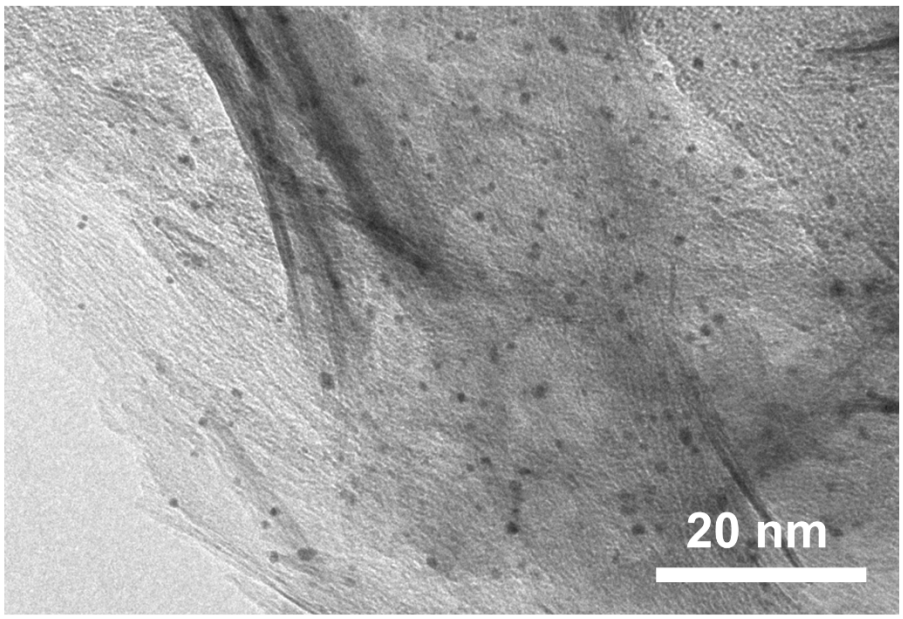

Figure S14. TEM image of recycled Pt clu/dp-Al_2O_3.

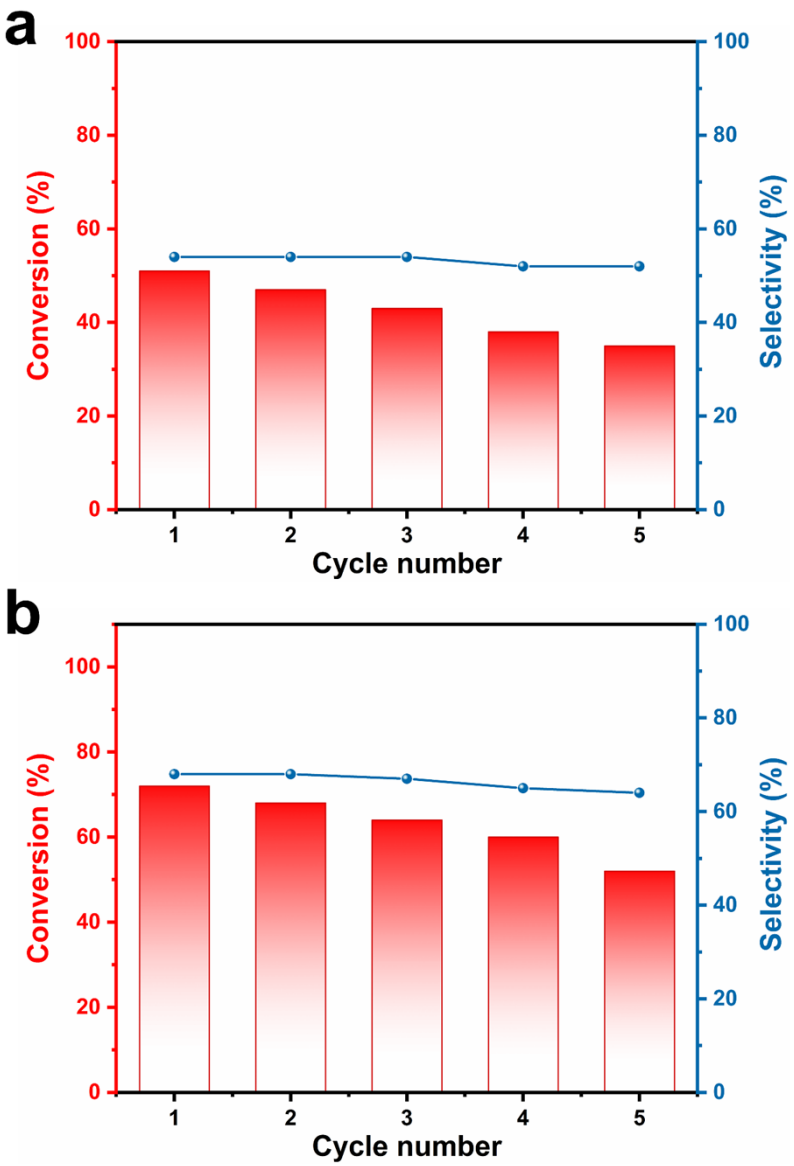

Figure S15. Catalytic performance of (a) Pt NPs/c-Al_2O_3 and (b) Pt clu/ c-Al_2O_3 for several recycles of repeated reactions.

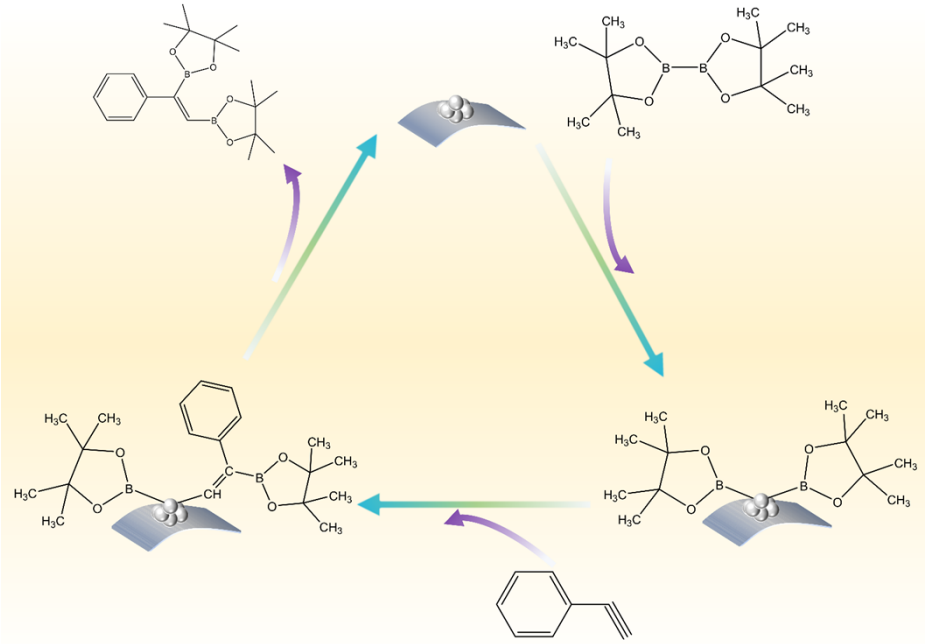

Figure S16. Reaction mechanism for phenylacetylene diboration over Pt clu/dp-Al_2O_3. The diboration reaction facilitated by the catalyst involves three primary steps: (1) the oxidative addition of the B-B bond and subsequent coordination with the Pt clusters, (2) the cleavage of the Pt-B bond and subsequent addition reaction with the C-C multiple bond, and (3) the reductive elimination of the C-B bond from Pt. The intermediates formed by the connection of Pt clusters with reactants are charge-asymmetric sites.

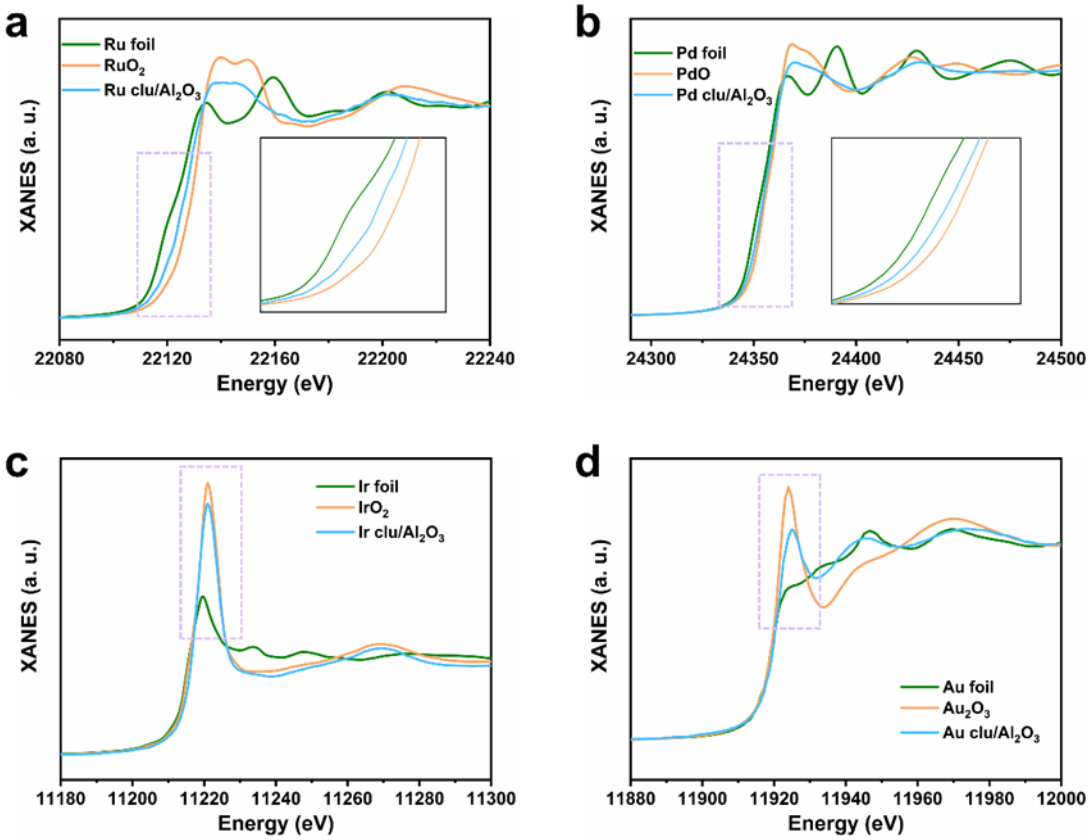

Figure S17. XANES of different elements of M clu/dp-Al_2O_3. (a) Ru clu/dp-Al_2O_3. (b) Pd clu/dp-Al_2O_3. (c) Ir clu/dp-Al_2O_3. (d) Au clu/dp-Al_2O_3.

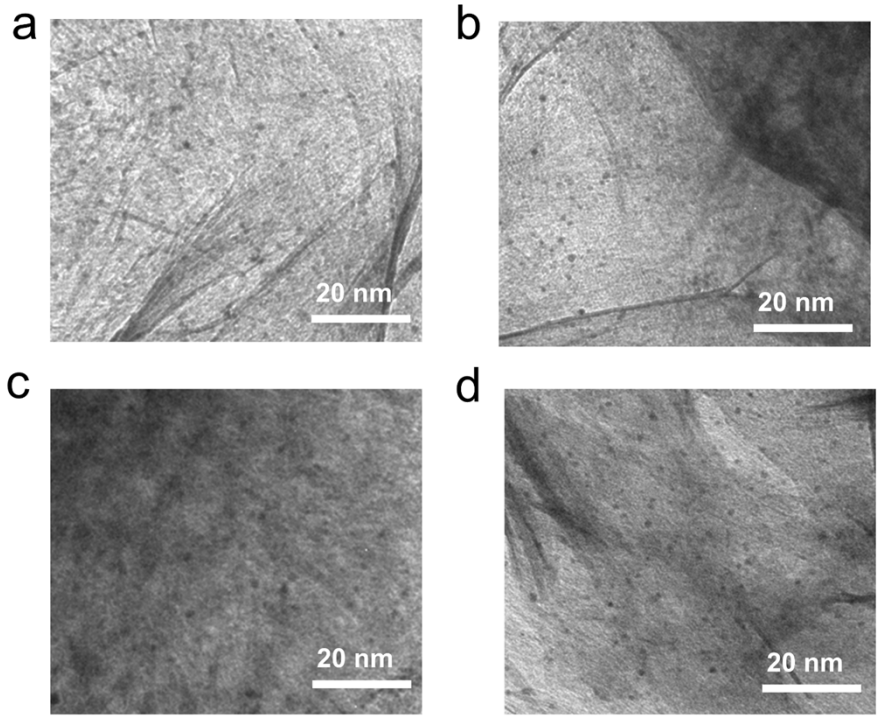

Figure S18. The TEM images of M clu/dp-Al_2O_3. (a) The TEM images of Ru clu/dp-Al_2O_3. (b) The TEM images of Pd clu/dp-Al_2O_3. (c) The TEM images of Ir clu/dp-Al_2O_3. (d) The TEM images of Au clu/dp-Al_2O_3.

Table S1. Structural parameters extracted from Pt L_3-edge EXAFS fitting. (S_0^2=0.84).

Sample	Path	CN	R(Å)	$\sigma^2(10^{-3}Å^2)$	ΔE_0(eV)	R factor
Pt clu/dp-Al_2O_3	Pt-O	1.9±0.4	2.01±0.01	7.1±0.8	5.2±0.4	0.007
	Pt-Pt	4.6±0.8	2.75±0.01	7.0±0.5		
	Pt-Pt_1	3.6±0.6	2.76±0.01	6.8±0.7	4.2±0.4	0.006
	Pt-Pt_2	2.2±0.4	2.73±0.01	7.3±0.5		
Pt foil	Pt-Pt	12*	2.78±0.01	5.0±0.3	8.3±0.5	0.004

S_0^2 is the amplitude reduction factor; CN is the coordination number; R is interatomic distance (the bond length between Pt central atoms and surrounding coordination atoms); σ^2 is Debye-Waller factor (a measure of thermal and static disorder in absorber-scatterer distances); ΔE_0 is edge-energy shift (the difference between the zero kinetic energy value of the sample and that of the theoretical model). R factor is used to value the goodness of the fitting.

* This value was fixed during EXAFS fitting, based on the known structure.

Error bounds that characterize the structural parameters obtained by EXAFS spectroscopy were estimated as N ± 20%; R ± 1%; σ^2 ± 20%; ΔE_0 ± 20%.

Table S2 Structural parameters of M (Ru, Pd, Ir, and Au) clu/dp-Al_2O_3 extracted from EXAFS fitting. (S_0^2=0.85).

Sample	Path	CN	R(Å)	$\sigma^2(10^{-3}Å^2)$	ΔE_0(eV)	R factor
Ru clu/dp-Al_2O_3	Ru-O	4.4±0.7	1.97±0.01	0.74±0.12	6.2±0.7	0.004
	Ru-Ru	2.4±0.4	2.68±0.01	0.55±0.08		
Pd clu/dp-Al_2O_3	Pd-O	3.9±0.6	2.01±0.01	2.8±0.09	7.3±0.6	0.007
	Pd-Pd	1.8±0.5	2.74±0.01	0.8±0.11		
Ir clu/dp-Al_2O_3	Ir-O	3.2±0.4	2.10±0.02	0.9±0.10	4.6±0.4	0.006
	Ir-Ir	2.5±0.7	2.67±0.01	3.2±0.26		
Au clu/dp-Al_2O_3	Au-O	1.6±0.2	1.98±0.01	5.2±1.0	-2.1±0.4	0.004
	Au-Au	3.4±0.3	2.86±0.01	3.4±0.06		

S_0^2 is the amplitude reduction factor; CN is the coordination number; R is interatomic distance (the bond length between central atoms and surrounding coordination atoms), σ^2 is Debye-Waller factor (a measure of thermal and static disorder in absorber-scatterer distances); ΔE_0 is edge-energy shift (the difference between the zero kinetic energy value of the sample and that of the theoretical model). R factor is used to value the goodness of the fitting.